Contributions to Mineralogy and Petrology (2018) 173:20
https://doi.org/10.1007/s00410-018-1443-8

ORIGINAL PAPER

Behaviour of Fe_4O_5–$Mg_2Fe_2O_5$ solid solutions and their relation to coexisting Mg–Fe silicates and oxide phases

Laura Uenver-Thiele[1] · Alan B. Woodland[1] · Nobuyoshi Miyajima[2] · Tiziana Boffa Ballaran[2] · Daniel J. Frost[2]

Received: 13 November 2017 / Accepted: 23 January 2018 / Published online: 9 February 2018

Abstract

Experiments at high pressures and temperatures were carried out (1) to investigate the crystal-chemical behaviour of Fe_4O_5–$Mg_2Fe_2O_5$ solid solutions and (2) to explore the phase relations involving $(Mg,Fe)_2Fe_2O_5$ (denoted as O_5-phase) and Mg–Fe silicates. Multi-anvil experiments were performed at 11–20 GPa and 1100–1600 °C using different starting compositions including two that were Si-bearing. In Si-free experiments the O_5-phase coexists with Fe_2O_3, hp-$(Mg,Fe)Fe_2O_4$, $(Mg,Fe)_3Fe_4O_9$ or an unquenchable phase of different stoichiometry. Si-bearing experiments yielded phase assemblages consisting of the O_5-phase together with olivine, wadsleyite or ringwoodite, majoritic garnet or Fe^{3+}-bearing phase B. However, $(Mg,Fe)_2Fe_2O_5$ does not incorporate Si. Electron microprobe analyses revealed that phase B incorporates significant amounts of Fe^{2+} and Fe^{3+} (at least ~ 1.0 cations Fe per formula unit). Fe-$L_{2,3}$-edge energy-loss near-edge structure spectra confirm the presence of ferric iron [$Fe^{3+}/Fe_{tot} = \sim 0.41(4)$] and indicate substitution according to the following charge-balanced exchange: $[4]Si^{4+} + [6]Mg^{2+} = 2Fe^{3+}$. The ability to accommodate Fe^{2+} and Fe^{3+} makes this potential "water-storing" mineral interesting since such substitutions should enlarge its stability field. The thermodynamic properties of $Mg_2Fe_2O_5$ have been refined, yielding $H°_{1bar,298} = -1981.5$ kJ mol^{-1}. Solid solution is complete across the Fe_4O_5–$Mg_2Fe_2O_5$ binary. Molar volume decreases essentially linearly with increasing Mg content, consistent with ideal mixing behaviour. The partitioning of Mg and Fe^{2+} with silicates indicates that $(Mg,Fe)_2Fe_2O_5$ has a strong preference for Fe^{2+}. Modelling of partitioning with olivine is consistent with the O_5-phase exhibiting ideal mixing behaviour. Mg–Fe^{2+} partitioning between $(Mg,Fe)_2Fe_2O_5$ and ringwoodite or wadsleyite is influenced by the presence of Fe^{3+} and OH incorporation in the silicate phases.

Keywords Fe_4O_5 · $Mg_2Fe_2O_5$ · Phase B · Phase relations · Deep mantle · High pressure · High temperature

Introduction

Over the past few years, post-spinel phases have attracted more and more attention due to the discovery of several high-pressure (hp) oxide phases with stoichiometries other than M_3O_4. Phases with M_4O_5, M_5O_6 and M_7O_9 stoichiometry have now been added to the list of potential post-spinel phases that might be present in the Earth's deep upper mantle and transition zone (e.g., Enomoto et al. 2009; Lavina et al. 2011; Lavina and Meng 2015; Woodland et al. 2012, 2013, 2015; Guignard and Crichton 2014; Ishii et al. 2014, 2015; Myhill et al. 2016; Sinmyo et al. 2016; Uenver-Thiele et al. 2017a, b). Phases with an M_4O_5 stoichiometry (O_5-phase) were found in a number of simple chemical systems, including those containing Cr, Al, Fe^{3+} as trivalent cations, and Mg and Fe^{2+} as divalent cations (e.g., Enomoto et al. 2009; Woodland et al. 2012, 2013; Ishii et al. 2014, 2015; Uenver-Thiele et al. 2017a, b). Often the O_5-phase occurs in an $M_4O_5 + M_2O_3$ post-spinel assemblage, as in the case of $Fe_4O_5 + Fe_2O_3$, $FeMgFe_2O_5 + Fe_2O_3$, $Fe_2Cr_2O_5 + Cr_2O_3$ or $Fe_2Cr_2O_5 + Cr_2O_3$ becoming stable at the expense of the spinel-structured phase at conditions of the deep upper mantle (Woodland et al. 2012; Ishii et al. 2014, 2015; Uenver-Thiele et al. 2017a, b).

Communicated by Jochen Hoefs.

Electronic supplementary material The online version of this article (https://doi.org/10.1007/s00410-018-1443-8) contains supplementary material, which is available to authorized users.

✉ Laura Uenver-Thiele
Uenver-Thiele@em.uni-frankfurt.de

[1] Institut für Geowissenschaften, Goethe-Universität Frankfurt, Altenhöferallee 1, 60438 Frankfurt, Germany

[2] Bayerisches Geoinstitut, Universität Bayreuth, 95440 Bayreuth, Germany

Solid solutions involving the Fe_4O_5 component are of particular interest because the ability to contain both Fe^{2+} and Fe^{3+} makes their stability sensitive to redox processes. The incorporation of Mg into Fe_4O_5 was first reported by Woodland et al. (2013); Boffa Ballaran et al. (2015) subsequently demonstrated that Mg can completely substitute for Fe^{2+}, producing an Mg endmember, $Mg_2Fe_2O_5$. Both endmember compositions share the same space group *Cmcm* with a $CaFe_3O_5$-type structure (Lavina et al. 2011; Boffa Ballaran et al. 2015), suggesting that the entire Mg–Fe^{2+} solid solution series is stable at high pressures and temperatures. Myhill et al. (2016) questioned whether Fe_4O_5 could occur in a peridotitic upper mantle or transition zone environment since their preliminary calculations implied that its stability required an oxygen fugacity that exceeded the expected mantle range (e.g., Frost and McCammon 2008). However, such a conclusion was based upon incomplete knowledge of potential phase assemblages, particularly those with Mg-rich silicates. In addition, even if such a situation were generally true, this does not rule out the stability of an O_5-phase in localized environments, such as those responsible for diamond formation where olivine and pyroxene do not coexist. In fact the microtexture of magnetite in an inclusion in diamond described by Jacob et al. (2016) led Uenver-Thiele et al. (2017b) to conclude that this magnetite was originally Fe_4O_5 at the conditions of diamond formation.

The recent investigations of the phase relations for $MgFe_2O_4$ and $Mg_{0.5}Fe_{0.5}Fe_2O_4$ by Uenver-Thiele et al. (2017a, b) also place important constraints on the stability of the $Mg_2Fe_2O_5$ endmember and the $MgFeFe_2O_5$ composition. However, knowledge of the properties of $(Mg,Fe)_2Fe_2O_5$ solid solutions and the phases with which they can coexist under mantle-relevant conditions remains incomplete. Thus, the purpose of this study is twofold: (1) to address the crystal-chemical behaviour of the Fe_4O_5–$Mg_2Fe_2O_5$ join and (2) to further investigate the phase assemblages in which an O_5-phase is stable, including those involving high-pressure Mg–Fe silicates.

Methods

High-pressure experiments

Five different starting compositions were employed in this study (Tables 1, 2). A starting mixture of $MgO + MgFe_2O_4$

Table 1 Conditions and run products of Si-free experiments conducted with Mg–Fe oxides

Experiment	Pressure (GPa)	Temperature (°C)	Run duration (h)	Run products[a]
$MgO + MgFe_2O_4$ composition				
M566	12	1300	5	hem + O_5 + UQ-O_8
Z1584u[b]	15	1600	2	O_5 + UQ-O_7
Z1233[b]	15	1600	3	O_5 + UQ-O_9 + (hem)
Z1234u[b]	20	1400	3	O_5 + (per)
$MgFe_2O_4$ composition				
M519	12	1300	4	O_5 + hem + UQ
Z1463o[b,c]	14	1400	3	O_5 + hem
Z1461o[b,c]	16	1300	3	per + hem + O_5
Z1234o[b,d]	20	1400	3	hp-O_4 + (O_5) + (hem)
H4349[b,d]	20	1500	2.5	hp-O_4 + (O_5) + (hem)
$Mg_{0.50(2)}Fe_{0.50(2)}Fe_2O_4$ composition				
M638[d]	11	1000	4	O_5 + hem
M645[d]	11	1200	3.5	O_5 + hem
M646[d]	12	1400	3.75	O_5 + hem
M648[d]	13	1500	2	O_5 + hem + (O_9)
M655	12	1600	1	O_5 + hem
Z1586o[d]	14	1100	3.5	O_5 + hem

[a] *O_4* (Mg,Fe)Fe_2O_4, *hem* hematite, *per* periclase, *hp-O_4* high-pressure polymorph of (Mg,Fe)Fe_2O_4, *O_5* $(Mg,Fe)_2Fe_2O_5$, *O_9* $(Mg,Fe)_3Fe_4O_9$, *UQ* unquenchable phase with undifferentiated stoichiometry, see text; *UQ-O_7* unquenchable phase with a possible stoichiometry of $Mg_4Fe_2O_7$, *UQ-O_8* unquenchable phase with a possible stoichiometry of $Mg_5Fe_2O_8$, *UQ-O_9* unquenchable phase with a possible stoichiometry of $Mg_6Fe_2O_9$; phases in parentheses are present in traces

[b] Experiments with added PtO_2

[c] Experiments reported in Uenver-Thiele et al. (2017a)

[d] Experiments reported in Uenver-Thiele et al. (2017b)

Table 2 Experimental conditions and run products for the MgO–FeO–Fe_2O_3–SiO_2 system

Experiment	Pressure (GPa)	Temperature (°C)	Run duration (h)	Run products[a]
0.7 $MgFe_2O_4$ + 0.3 Mg_2SiO_4				
Z1586u	14	~1100 ± 100	3.5	O_5 + ol[c] + Fe^{3+}-phase B + (wads)
Z1532u[b]	16	1400	3.5	O_5 + wads[c] + (rgw) + (mgs)[c]
Z1587o	20	1200	3.5	O_5 + rgw[c] + Fe^{3+}-phase B[c]
Z1531o[b]	20	1350	4	O_5 + wads[c] + (mgs)
0.75 $MgSiO_3$ + 0.25 Fe_2O_3				
Z1507o	20	1600	2	O_5 + grt[c] + rgw

[a]Run product abbreviation: *O_5* (Mg,Fe)Fe_2O_5, *wads* wadsleyite, *ol* olivine, *Fe^{3+}-phase B* Fe^{3+}-bearing phase B, *rgw* ringwoodite; phases in parentheses are present only in traces

[b]Experiments with added PtO_2

[c]Confirmed by Raman spectroscopy

in a 1:1 molar ratio as well as pre-synthesized $MgFe_2O_4$ and $Mg_{0.5}Fe_{0.5}Fe_2O_4$ were employed to investigate the crystal-chemical behaviour of solid solutions along the Fe_4O_5–$Mg_2Fe_2O_5$ join (Table 1). The synthesis of magnesioferrite and $Mg_{0.5}Fe_{0.5}Fe_2O_4$ is reported in Uenver-Thiele et al. (2017a, b), respectively. A mixture of 70 mol% $MgFe_2O_4$ and 30 mol% Mg_2SiO_4 was used to investigate equilibria involving $Mg_2Fe_2O_5$ and high-pressure Si-bearing phases (Table 2). Another starting mixture of 75 mol% $MgSiO_3$ and 25 mol% Fe_2O_3 (Table 2), giving a composition of $Mg_3Fe_2Si_3O_{12}$, was produced by combining sintered hematite with enstatite glass. The glass was produced by melting a stoichiometric mixture of MgO and SiO_2 in a Pt-crucible at 1660 °C using a high-temperature furnace for 1 h. It was quenched in ice water and re-grounded for a second cycle of melting at 1650 °C for a further 20 min. This procedure yielded a clear glass with no microscopic quench crystals.

Experiments up to 13 GPa were performed with a 800-t Walker-type multi-anvil press at the University of Frankfurt. Pressure calibration and pressure cell design are given in Brey et al. (2008). Temperature was monitored by W_5Re_{95}–$W_{26}Re_{74}$ thermocouples with the electromotive force uncorrected for pressure. Capsule designs follow those described in Uenver-Thiele et al. (2017a). For experiments at pressures ≥ 14 GPa, 5000-t and 1000-t multi-anvil presses were employed at the Bayerisches Geoinstitut, Bayreuth. The experimental setup and pressure calibration are described in Keppler and Frost (2005). High-pressure assemblies with a $LaCrO_3$ heater were employed with the temperature monitored by W_3Re_{97}–$W_{25}Re_{75}$ thermocouples with the electromotive force uncorrected for pressure. Uncertainties in pressure and temperature are ± 0.5 GPa and ± 30–50 °C, respectively (Keppler and Frost 2005). Samples were packed into Pt-foil capsules, except for experiment Z1507o that employed Ag-foil as capsule material. Several experiments were conducted with small amounts of PtO_2 to avoid reduction of ferric iron. In others, PtO_2 was omitted since we intended to produce mixed-valence Fe^{3+}–Fe^{2+}-bearing solid solutions. The high oxygen fugacity of the experiments as imposed by the high Fe^{3+} contents of the starting materials meant that Fe-loss to the Pt capsule was negligible. The experiments were first cold pressurized, followed by heating to the desired temperature. They were terminated by turning off the power to the heater, but maintaining the pressure. Decompression was then immediately initiated. The resulting run products, as well as experimental run conditions are reported in Tables 1 and 2.

Analytical techniques

Recovered samples were characterized primarily by electron microprobe (EPMA) and powder X-ray diffraction, with selected samples also investigated by transmission electron microscopy (TEM) and micro-Raman spectrometry. Fragments of sample material were embedded in epoxy and polished for EPMA analysis. Measurements were performed at the University of Frankfurt using a five-spectrometer JEOL JXA-8900 superprobe operating in the wavelength-dispersive mode (at 15 kV, 20 nA, 1 µm spot size). Pure MgO, Fe_2O_3, Pt and $CaSiO_3$ were used as primary standards. Integration times for Si and Mg were 40 s on the peak and background, while for Fe and Pt an integration time of 40 s on the peak and 20 s on the background was employed. For experiment Z1507o, forsterite (Mg), fayalite (Fe) and wollastonite (Si) were employed as standards. Integration times for Mg, Fe and Si were the same as described above. A CITZAF algorithm was employed for matrix correction (Armstrong 1993).

Powder X-ray diffraction patterns were obtained on a STOE Stadi P diffractometer operating at 45 kV and 35 mA with monochromatic Mo Kα ($\lambda = 0.70926$ Å) radiation, equipped with a linear PSD or a Mythen detector at the University of Frankfurt. An internal Si standard was added to the sample material and mounted in a 0.5-mm-diameter capillary.

Diffraction patterns were collected in transmission mode between 1°–100° 2θ. Several samples were analysed using a Philips X´Pert PRO diffractometer at the Bayerisches Geoinstitut. Co Kα1 ($\lambda = 1.78897$ Å) radiation, monochromated with a symmetrically cut curved Johansson Ge (111) crystal and a Philips X'celerator detector were employed. A small amount of Si powder was added to the sample as an internal standard and mounted on a silicon wafer. Data collection was performed in reflection mode at 40 kV and 40 mA and between 10° and 120° 2θ. The diffraction patterns were analysed with the General Structure Analysis System (GSAS, Larson and van Dreele 1994) software package with the EXPGUI interface of Toby (2001) for phase identification and determination of the unit-cell parameters for the $(Mg,Fe)_2Fe_2O_5$ solid solutions.

For selected samples, further phase identification was performed using a Renishaw micro-Raman spectrometer (RM-1000) equipped with a 633 nm HeNe laser at the University of Frankfurt. The 519 cm^{-1} peak of a Si wafer was used for calibration (Temple and Hathaway 1973). Unpolarized confocal Raman spectra were collected with a 50x microscope objective and a laser power of ~10 mW. The wavenumber accuracy was about ±2 cm^{-1}. The focused laser spot on the sample was approximately ~2 µm in diameter.

Transmission electron microscopic characterizations were carried out using a 200 kV Philips CM-20FEG TEM equipped with an energy-dispersive X-ray spectrometer (NO-RAN Ge detector) and a parallel electron energy-loss spectrometer (Gatan 666 PEELS). A small chip from sample Z1586u used in the X-ray diffraction measurement was crushed under ethanol and the dispersion was placed on a Lacey carbon film on Cu-grid. For textural as well as crystallographic investigations, conventional TEM techniques such as bright field (BF) and dark field (DF) imaging, as well as selected area electron diffraction (SAED) were employed. Chemical compositions were cross-checked by energy-dispersive X-ray (EDX) analyses. The Fe-$L_{2,3}$-edge electron energy-loss near-edge structure (ELNES) of the selected sample was also examined using spectra collected in diffraction mode with a collection semi-angle of $\beta = 2.7$ mrad, an energy-dispersion of 0.1 eV per channel and 10–20 s integration time per read-out. The energy resolution is 0.8–0.9 eV, measured as the full width of the zero-loss peak at half-maximum. Quantification of the Fe-$L_{2,3}$ ELNES followed the procedure described by van Aken et al. (1998) and van Aken and Liebscher (2002), using an empirically calibrated universal curve.

Results and discussion

Phase relations of $(Fe,Mg)_2Fe_2O_5$ solid solutions

In order to investigate the crystal-chemical behaviour of Fe_4O_5–$Mg_2Fe_2O_5$ solid solutions, six additional experiments were performed in the pressure–temperature range of 12–20 GPa and 1300–1600 °C to augment the data of Woodland et al. (2013) and Uenver-Thiele et al. (2017a, b). The conditions and run products from the experiments are summarized in Table 1, along with those experiments from Uenver-Thiele et al. (2017a, b) for which unit-cell parameters and the molar volumes for the O_5-phase are presented here for the first time. Representative electron microprobe analyses of each phase synthesized in the six new experiments are listed in Table 3.

In most experiments, the O_5-phase occurs with hematite, except for two cases where an "O_5" bulk composition was used (Table 1; samples Z1584u and Z1234u). Some samples contain a coexisting unquenchable phase (UQ) that exhibits a mottled texture in backscattered electron (BSE) images (Fig. 1a–c), indicating breakdown during decompression. However, the UQ-phase is marked by straight grain boundaries of larger crystals with 120° triple junctions implying that equilibrium was attained during the experiment (see Fig. 1a-c). The bulk composition of the UQ-phase was determined from 4 µm diameter spot analyses, revealing homogenous compositions with only minor variations for each sample (Table 3). Different stoichiometries were obtained (Tables 1, 3) depending on the experimental run conditions. For example, in experiment M519 $(Mg,Fe)_2Fe_2O_5$ and hematite occur up to 30 µm in size and coexist together with an interstitial UQ-phase (Table 1; Fig. 1b, c). However, the mottled texture indicative of decomposition is not complete and relict domains of the original phase are apparent in BSE images (e.g., Fig. 1c). Microprobe analyses were performed in both parts of these grains; a "normal" spot size (1 µm) for the un-mottled part and a larger 4 µm spot for the mottled region (Fig. 1c). The compositions of these two regions are in perfect agreement with each other, yielding 38.97(25) wt% MgO and 52.88(44) FeO for the relict parts and 39.35(4) wt% MgO and 52.85(23) wt% FeO, for the mottled parts, respectively (Table 3). Reflections in the X-ray powder diffraction pattern also confirm the presence of a phase in addition to $(Mg,Fe)_2Fe_2O_5$, hematite, (Mg,Fe)O and magnesioferrite, the latter two of which are decomposition products (see Uenver-Thiele et al. 2017a). Extra reflections, corresponding to *d*-values of about 2.967 and 1.713 Å are observed and do not match any of the known Mg–Fe-oxide phases. It is likely that these reflections belong to the relict phase identified in the BSE images. Unfortunately, further analysis of the crystal structure of this phase is currently hampered by its apparent instability at ambient pressure and by overlapping peaks in the powder diffraction pattern. Assessing the stoichiometry of this relict phase is also ambiguous since no PtO_2 was added to the experiment and the composition of the coexisting O_5-phase of $Mg_{1.53(1)}Fe_{0.47(1)}Fe_2O_5$ indicates that

Table 3 Chemical analyses of run products of Si-free experiments obtained by EPMA

Sample	M519	M519	M519	M566	M566	M566	M655	Z1233	Z1233	Z1234u	Z1234u	Z1584u	Z1584u
MgO	24.3(2)	39.0(3)	39.35(4)	2.26(1)	1.92(7)	28.4(1)	52.8(4)	9.6(2)	33.2(2)	61.4(2)	33.91(1)	90.2(1)	30.7(1)	49.9(6)
FeO	70.4(3)	52.9(4)	52.9(2)	86.9(4)	87.7(4)	67.9(3)	43.9(9)	86.2(4)	62.5(3)	34.6(1)	61.8(3)	10.2(4)	64.9(4)	46.4(8)
PtO_2	b.d.l	0.02(1)	b.d.l	b.d.l	b.d.l	b.d.l	b.d.l	b.d.l	b.d.l	0.21(1)	0.09(5)	0.02(4)	0.56(11)	0.2(1)
Totals	94.6(6)	91.9(7)	92.2(3)	89.2(3)	89.6(5)	96.3(4)	96.6(8)	95.7(3)	96.8(4)	96.2(1)	95.8(4)	100.4(5)	96.3(4)	97.2(5)
Comment	(Mg,Fe) Fe_2O_5	UQ-phase? no mottling[a]	UQ-phase? w/mottling[b]	hem	hem	(Mg,Fe) Fe_2O_5	$UQ\text{-}O_8$?	(Mg,Fe) Fe_2O_5	$UQ\text{-}O_9$?	(Mg,Fe) Fe_2O_5	per	(Mg,Fe) Fe_2O_5	$UQ\text{-}O_7$?	

[a] Area analysed without mottled texture

[b] Area analysed with mottled texture

Fig. 1 Back scatter electron (BSE) images of the run products from experiment Z1584u (**a**), exhibiting well developed crystals of $(Mg,Fe)_2Fe_2O_5$ together with an unquenchable phase (UQ). Here, $(Mg,Fe)_2Fe_2O_5$ is the most abundant phase exhibiting straight grain boundaries and triple junctions between individual grains. Hematite is present as small interstitial grains or has the same dimension as $(Mg,Fe)_2Fe_2O_5$. The run products produced in experiment M519, **b, c** indicate the assemblage of $(Mg,Fe)_2Fe_2O_5$ + UQ phase + hematite. The unquenchable phase also exhibits straight grain boundaries and triple junctions that are preserved from before the quench (**b**). However, mottled textures in the inner part of the grains point to partial decomposition during decompression of the experiment (**c**). The four different circles indicated in **c** show the position and the spot size used for microprobe analyses within mottled and relict domains of the unquenchable phase

some reduction of ferric to ferrous iron occurred during the experiment. Thus, a number of stoichiometries, each with different Fe^{3+}/Fe^{2+} would be consistent with the observed bulk composition from EPMA. However, combining the robust measure of Mg/Fe_{tot} for this phase along with possible phase field topologies with a coexisting O_5-phase and hematite place some constraints on its stoichiometry (Fig. 2). For example, an O_9-stoichiometry with composition $Mg_{4.55}Fe_{1.45}Fe_2O_9$ would be essentially collinear with the O_5-phase and hematite in the system MgO–FeO–$FeO_{1.5}$, indicating that the three phases cannot be in equilibrium (Fig. 2). In addition, any phases containing more Fe^{2+} than the $A_6B_2O_9$ stoichiometry should not be in equilibrium with hematite. This leaves $Mg_{2.85}Fe_{0.15}Fe_2O_6$, $Mg_{3.42}Fe_{0.58}Fe_2O_7$ or $Mg_{3.99}Fe_{1.01}Fe_2O_8$ as potential compositions (Fig. 2), all stoichiometries that have already been suggested to have narrow stability fields in the Fe^{2+}-free MgO–$FeO_{1.5}$ binary system at pressures of 10–13 GPa and temperatures ≥ 1200 °C (Uenver-Thiele et al. 2017a). On the other hand, such an UQ-phase was not found in experiments conducted with a $(Mg_{0.5}Fe_{0.5})Fe_2O_5$ bulk composition (Uenver-Thiele et al. 2017b). Thus, the phase assemblage observed in sample M519 is important in that it indicates the possibility that a variety of Fe^{3+}-bearing oxide stoichiometries may be stable at high pressures and temperatures, even if Fe^{2+} apparently acts to destabilize some of these structures (like observed for wadsleyite; e.g., Fig. 3).

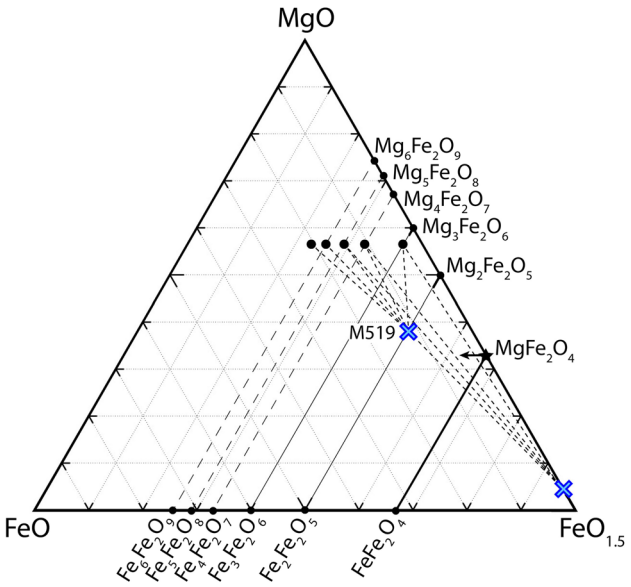

Fig. 2 Ternary diagram for the MgO–FeO–$FeO_{1.5}$ system illustrating the possible phase relations for sample M519. Without explicitly knowing the nature of the unquenchable phase (UQ), a number of stoichiometries with different Fe^{3+}/Fe^{2+}, but constant Mg/Fe_{tot} are consistent with the microprobe analyses. However, the topologies of the coexisting phase fields place some constraint on the stoichiometry of the UQ phase (see text)

Mg–Fe silicates coexisting with $(Mg,Fe)_2Fe_2O_5$

Five experiments were performed to further explore phase relations involving the O_5-phase and Mg–Fe silicates at high pressures and temperatures (Table 2). The combination of BSE imaging and EPMA analyses reveals at least three phases coexisting in these experiments (Tables 2, 4). The most abundant phase is $(Mg,Fe)_2Fe_2O_5$, which does not incorporate Si in its structure, in agreement with previous observations (e.g., Woodland et al. 2013; Bindi et al. 2016). In the X-ray powder diffraction patterns, $(Mg,Fe)_2Fe_2O_5$ could be indexed using the crystal structure model reported by Boffa Ballaran et al. (2015). Raman spectra of the O_5-phase exhibit two characteristic peaks at ~ 315 and ~ 673 cm^{-1}, along with several other overlapping peaks lying between 450 and 550 cm^{-1} (Electronic Supplementary Material S.1).

As anticipated, an additional phase having $(Mg,Fe)_2SiO_4$ stoichiometry was identified by EPMA (see Table 4) and characterized by means of X-ray diffraction and/or Raman spectroscopy. Considering that many diffraction peaks of the three $(Mg,Fe)_2SiO_4$ polymorphs: olivine, wadsleyite and ringwoodite overlap with those of the O_5-phase, Raman spectra often proved to be particularly useful in phase identification by comparing them with spectra from McMillan and Akaogi (1987) and Guyot et al. (1986).

The occurrence of olivine, wadsleyite or ringwoodite is consistent with the phase relations of Mg_2SiO_4–Fe_2SiO_4 solid solutions at high pressure and temperature (Katsura and Ito 1989, see Fig. 3). One exception is the presence

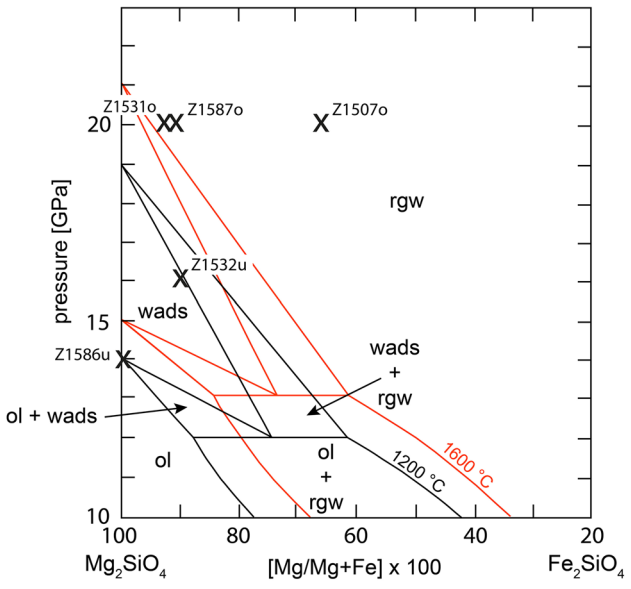

Fig. 3 Experimental data plotted along with calculated stability fields for olivine (ol), wadsleyite (wds) and ringwoodite (rgw) (after Katsura and Ito 1989) in the Mg_2SiO_4–Fe_2SiO_4 system

Table 4 Chemical analyses of run products of Si-bearing experiments obtained by EPMA

Sample	Z1507o	Z1507o	Z1507o	Z1531o	Z1531o	Z1532u	Z1532u	Z1586u	Z1586u	Z1586u	Z1587o	Z1587o	Z1587o
SiO_2	53.3(1)	36.47(4)	0.87(1)	39.9(1)	0.25(1)	0.32(2)	38.0(2)	29.9(3)	0.04(1)	42.2(3)	30.6(5)	40.9(2)	0.14(6)
MgO	28.8(1)	33.0(2)	7.73(3)	50.4(1)	22.1(1)	21.9(3)	47.6(3)	59.2(3)	13.19(7)	56.7(6)	59.9(3)	50.23(9)	15.9(2)
FeO	18.2(2)	31.75(3)	87.0(4)	10.2(1)	73.7(4)	73.3(5)	14.4(3)	9.9(5)	83.47(8)	2.2(6)	8.5(2)	10.5(2)	80.9(2)
PtO_2	n.a	n.a	n.a	0.06(8)	0.04(7)	0.1(1)	0.04(5)	b.d.l	b.d.l	0.1(1)	n.a	n.a	n.a
Totals	100.33	101.21	95.60	100.58	96.10	95.62	100.04	98.93	96.70	101.20	98.97	101.63	96.94
X_{Mg}	0.807	0.666	0.27	0.927	0.691	0.688	0.91	0.947	0.43	0.99	0.954	0.908	0.52
Comment	grt	rgw	$(Fe,Mg)_2Fe_2O_5$	wads	$(Fe,Mg)_2Fe_2O_5$	$(Fe,Mg)_2Fe_2O_5$	wads	Fe-phase B	$(Fe,Mg)_2Fe_2O_5$	ol	Fe-phase B	rgw	$(Fe,Mg)_2Fe_2O_5$

grt majoritic garnet, *rgw* ringwoodite, *wads* wadsleyite, *Fe-phase B* Fe^{3+}-bearing phase B, *ol* olivine, *n.a* not analysed, *b.d.l* below detection limit

of wadsleyite in experiment Z1531o conducted at 1350 °C and 20 GPa (Fig. 3). Considering the study of Mrosko et al. (2015), the occurrence of wadsleyite may be due to the incorporation of Fe^{3+} and OH. They reported that this combination significantly expands the wadsleyite stability field to higher pressures and higher Fe^{2+} contents at the expense of ringwoodite. In fact, Raman spectra of wadsleyite from this experiment reveal small peaks at ~3340 and 3580 cm^{-1}, which can be attributed to OH-stretching modes (Kleppe et al. 2005). These two bands were also observed in sample Z1532u, although their intensities were significantly lower. The origin of small amounts of H_2O in Z1531o and Z1532u could lie with the fact that small amounts of PtO_2 were added to both experiments. It is known that the very fine-grained PtO_2 powder can contain adsorbed atmospheric CO_2 as indicated by the presence of traces of magnesite in such experiments (Table 2; Uenver-Thiele et al. 2017a), and it is conceivable that small amounts of H_2O could also have been adsorbed on the PtO_2 as well.

Our new experiments are richer in Mg than those previously reported by Woodland et al. (2013) and demonstrate that $(Mg,Fe)_2Fe_2O_5$ can coexist with silicates having mantle-relevant compositions (i.e., with X_{Mg} = ~0.9). In two experiments (Z1531o, Z1532u), traces of magnesite were detected in the X-ray powder diffraction patterns. As suggested by Uenver-Thiele et al. (2017a), its presence is likely due to CO_2 adsorbed onto the PtO_2 powder (see above). The coexistence of $(Mg,Fe)_2Fe_2O_5$ solid solutions with several silicate phases (olivine, wadsleyite, ringwoodite, clinopyroxene) or oxides (spinel and spinelloid V) was previously reported by Woodland et al. (2013) for rather Fe-rich bulk compositions. From the results of experiment Z1507o (Table 3), we can now add majoritic garnet to the list of phases with which O_5-phase can coexist. Microprobe analyses (Table 4) indicate a composition of 82 mol% $(Mg,Fe)_4Si_4O_{12}$ and 18 mol% $(Mg,Fe)_3Fe_2Si_3O_{12}$. In the absence of other constraints, the actual apportioning of Fe^{2+} between the two garnet components is currently not possible.

Compared to other samples that have a homogenous distribution of phases, run products from Z1587o and Z1586u are marked by distinctly different textures (Fig. 4a, b). The O_5-phase forms large crystals and is most abundant, but there are two other phases with a lower mean atomic number Z illustrated by a lower contrast in BSE images (dark and middle grey). Olivine/wadsleyite (Z1586u) and ringwoodite (Z1587o) (dark grey in Fig. 4a, dark-middle grey in Fig. 4b) are almost entirely enclosed by another phase with a slightly different grey scale that contains distinctly less SiO_2 than the $(Mg,Fe)_2SiO_4$ polymorphs (Table 3). Investigation of sample Z1586u by TEM revealed nicely developed crystals (Fig. 5b) and selected area electron diffraction (SAED) patterns (Fig. 5a, c, d) could be indexed on the basis of a monoclinic cell (space group $P2_1/c$) with lattice parameters a = 10.6249(17),

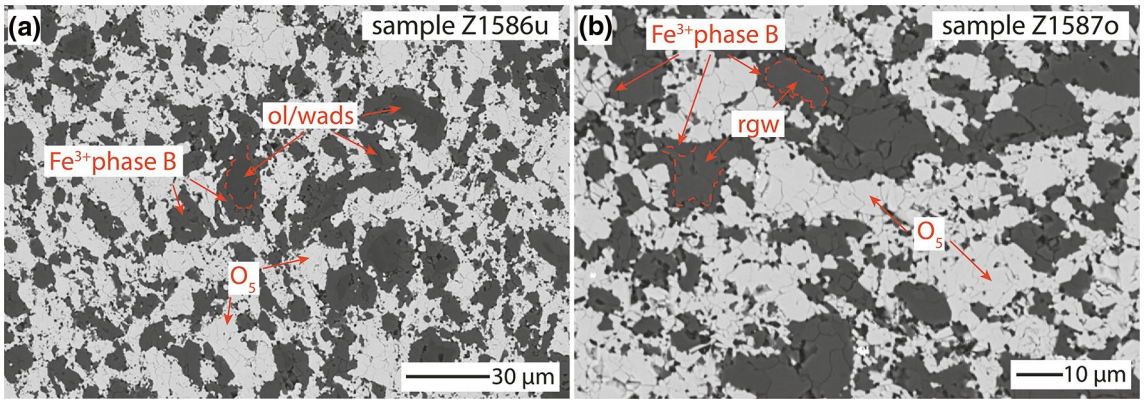

Fig. 4 BSE images of run products of experiments: **a** Z1586u and **b** Z1587o. In both cases, olivine or ringwoodite are enclosed by Fe^{3+}-bearing phase B. The sample consists of ~50% large crystals of $(Mg,Fe)_2Fe_2O_5$. In sample Z1586u, Fe^{3+}-bearing phase B is much more abundant than olivine and is not only associated with olivine. In this case, the Fe content of phase B is ~five times higher than in olivine. In sample Z1587o, phase B is as abundant as ringwoodite. However, both phases differ in their FeO content by only ~2 wt%, which explains the only slightly different contrast in the BSE image

$b = 14.1332(28)$, $c = 10.1015(18)$ Å and $\beta = 104.08(1)°$. This is consistent with phase B reported by Finger et al. (1989), which is surprising since no water was added to the experiment.

Raman spectra with peaks characteristic for phase B (McMillan et al. 1991; Liu et al. 1998) were subsequently obtained from samples Z1586u and Z1587o (Fig. 6). A number of the peaks are quite broad, which can be explained by the rather high Fe content of our samples (Table 4). Small peaks at ~3360 and 3412 cm^{-1} confirm the presence of OH groups in the structure.

EPMA measurements for the Fe-bearing phase B found in sample Z1586u gave a composition of $Mg_{11.17(4)}Fe_{1.04(6)}Si_{3.79(3)}O_{21}H_2$, which, from the deviation from 4 Si per formula unit, implies ~0.43(5) Fe^{3+} cations have entered the structure via the charge-balanced substitution: $^{[4]}Si^{4+} + {}^{[6]}Mg^{2+} = 2Fe^{3+}$. Fe-$L_{2,3}$-edge energy-loss near-egde structure (ELNES) spectra based on EELS measurements were taken from this phase (sample Z1586u) to evaluate the Fe^{3+}/Fe_{tot} ratio more quantitatively. The mixed valance state of iron was confirmed by the splitting in the white-lines, showing two separate Fe-$L_{2,3}$ maxima for ferrous and ferric iron (Fig. 7). The Fe^{3+}/Fe_{tot} ratios determined from the spectra vary from 0.35(4) to 0.46(4) in agreement with the stoichiometric calculation from EPMA analyses. To our knowledge, this is the first report of phase B incorporating significant amounts of Fe^{3+} and it is found to coexist with $(Mg,Fe)_2Fe_2O_5$ as well as with either olivine or ringwoodite.

Crystal-chemical behaviour of $(Mg,Fe)_2Fe_2O_5$ solid solutions

The range in composition obtained for Fe_4O_5–$Mg_2Fe_2O_5$ solid solutions in this study, combined with literature data

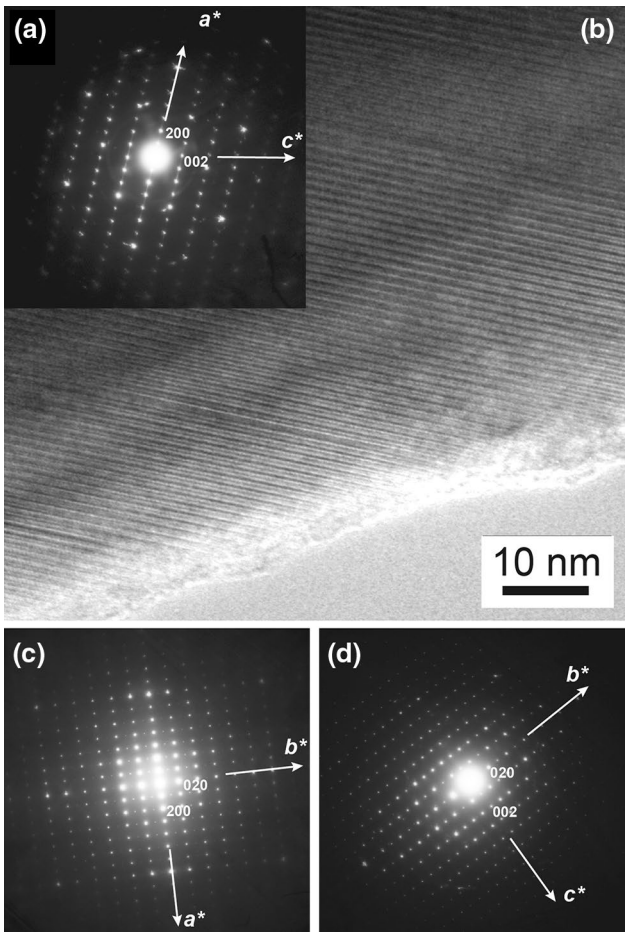

Fig. 5 **a** Selected area electron diffraction (SAED) pattern and **b** high-resolution TEM lattice image along the [010] zone axis of Fe^{3+}-bearing phase B from experiment Z1586u. Some stacking faults parallel to the (100) plane are visible. **c** SAED patterns along the [001] and **d** the [100] zone axes in the phase B structure, respectively

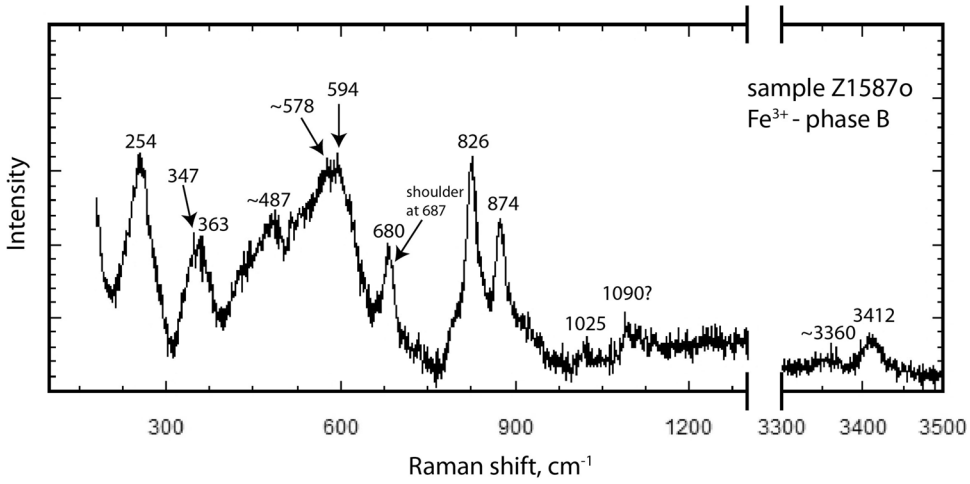

Fig. 6 Ambient Raman spectrum of Fe^{3+}-bearing phase B in sample Z1586u, with some structural OH revealed by small peaks at ~3360 and 3412 cm^{-1}

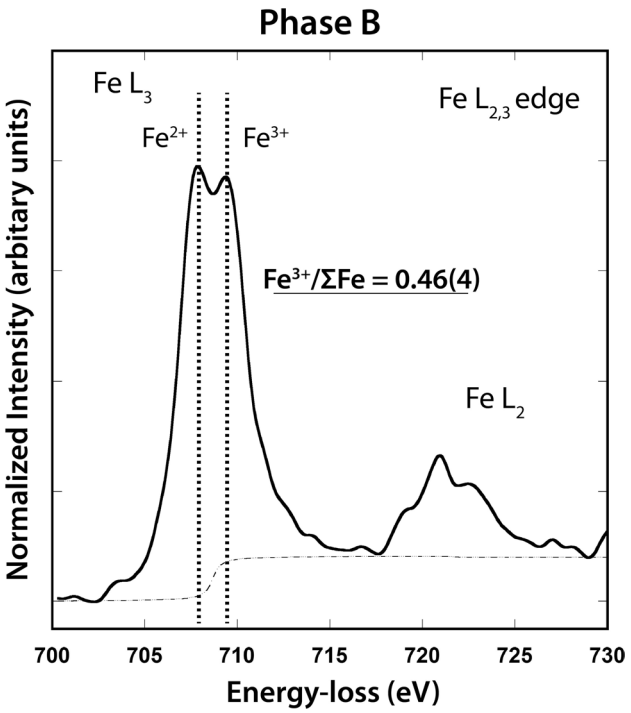

Fig. 7 Representative Fe-$L_{2,3}$-edge ELNES spectrum taken from phase B (sample Z1586u). The spectrum has been gain-normalized, background-subtracted and deconvoluted using the corresponding low-loss spectrum (not shown). The black dotted lines represent the position of the Fe-$L_{2,3}$ white-line maxima for Fe^{2+} (at ~707.8 eV, fixed for the energy calibration) and Fe^{3+} (~710 eV), respectively. The grey dashed line below the spectrum represents the double arctan background function. The $Fe^{3+}/\Sigma Fe$ quantification was made following the method of van Aken et al. (1998)

indicates that a complete solid solution exists across the binary join (see Table 5). Molar volumes decrease linearly with increasing Mg content (Fig. 8a). Application of symmetric or asymmetric solution models led to no statistical improvement in the fit to the data and the uncertainties in the interaction parameters were roughly equal to the derived values. Thus, we conclude that with the present uncertainties, the molar volumes vary essentially ideally across the binary. Extrapolation to the $Mg_2Fe_2O_5$ endmember composition yields a molar volume of 52.99(1) cm^3 (Fig. 8a), which is in agreement with the values reported from the single-crystal refinements of Boffa Ballaran et al. (2015) and Siersch et al. (2017).

The change in molar volume along the solid solution is primarily due to a near linear decrease of ~0.08 Å in the *b*-parameter with increasing Mg content (Fig. 8c), consistent with the observations of Woodland et al. (2013). Moreover, our more extensive dataset clearly indicates additional, more subtle changes in both the *a*- and *c*-parameters with composition (Fig. 8b, d), which could not be resolved by Woodland et al. (2013). Single-crystal structural refinement of the $Mg_2Fe_2O_5$ endmember reveals that Mg occupies all three crystallographic sites to various degrees, with a preference over Fe^{3+} for the M3 site (Boffa Ballaran et al. 2015). It is very likely that the large Fe^{2+} atom exhibits a similar site preference as Mg. Therefore the small changes in the *a*-parameter, which is controlled by the height of the M3 triangular prism, may be mainly due to Fe^{2+}–Mg substitution at the M3 site with little or no influence from Fe^{3+}. Even though the *c*-parameter is by far the largest in the unit-cell, it undergoes only ~25% of the shortening across the join compared to the *b*-parameter (Fig. 8b, d). These systematics can be understood by considering the following two effects of Mg–Fe^{2+} substitution on the structure of the Fe_4O_5–$Mg_2Fe_2O_5$ solid solutions: (1) the M2–O1–M2 angle formed by the only corner-sharing bonds in the structure can change (i.e., rotation of M2 octahedra) to accommodate some of the geometric effects of substituting a smaller Mg cation for Fe^{2+}, thereby compensating for some of the necessary shortening along the *c*-axis; (2) significant occupancy of M1 by Mg will have a strong influence on decreasing the M1–O2 bond distance, which principally leads to shortening of the *b*-parameter (Boffa Ballaran et al. 2015;

Table 5 Chemical composition, unit-cell parameters and molar volume of Fe_4O_5–$Mg_2Fe_2O_5$ solid solutions

Experimental run	$A_2B_2O_5$ nMg	nFe^{2+}	a (Å)	b (Å)	c (Å)	V (cm^3/mol)
Z1507	0.541(1)	1.500(1)	2.8917(4)	9.7827(21)	12.563(2)	53.507(9)
M655	0.663(7)	1.337(7)	2.8910(2)	9.7652(7)	12.5634(7)	53.397(3)
M645	0.838(10)	1.162(10)	2.8935(2)	9.7633(6)	12.5613(7)	53.423(3)
Z1586u	0.870(15)	1.134(19)	2.8942(1)	9.7553(3)	12.561(4)	53.392(2)
Z1586o	0.915(11)	1.085(11)	2.8931(2)	9.7592(8)	12.5584(8)	53.382(5)
M638	0.918(2)	1.082(2)	2.8936(2)	9.7591(9)	12.5582(9)	53.391(5)
M648	0.932(3)	1.068(3)	2.8932(3)	9.7593(10)	12.5581(10)	53.382(5)
M646	0.965(13)	1.035(13)	2.8927(2)	9.7602(6)	12.5581(7)	53.378(3)
Z1587o	1.033(10)	0.973(8)	2.8930(1)	9.7484(3)	12.559(3)	53.326(2)
Z1532u	1.386(6)	0.627(7)	2.8912(2)	9.7338(7)	12.5540(7)	53.191(3)
Z1531o	1.390(9)	0.621(8)	2.8910(1)	9.7275(4)	12.5590(5)	53.171(3)
M519	1.527(12)	0.473(12)	2.8926(1)	9.7408(7)	12.5551(7)	53.258(3)
M566	1.708(5)	0.292(5)	2.8919(6)	9.732(2)	12.554(2)	53.19(1)
Z1584u	1.829(7)	0.164(8)	–	–	–	–
Z1461o	1.885(1)	0.115(1)	2.8884(7)	9.7253(25)	12.5468(26)	53.06(1)
Z1463o	1.895(3)	0.105(3)	2.8872(2)	9.7228(8)	12.5523(9)	53.048(5)
Z1233	1.945(7)	0.055(7)	2.8862(2)	9.7180(8)	12.5520(8)	53.003(5)
H4349	1.975(3)	0.025(3)	–	–	–	–
Z1234u	1.978(5)	0.022(5)	2.8856(2)	9.7181(9)	12.5494(9)	52.982(5)

Woodland et al. 2013). The similarity in unit-cell parameters for $(Mg,Fe)_2Fe_2O_5$ solid solutions synthesized at different temperatures (see Tables 1, 2) suggests that the observed order–disorder behaviour is more a crystal-chemical phenomenon than being thermally induced or related to the quench process of the experiments.

Thermodynamic properties of $Mg_2Fe_2O_5$

In their study of high-pressure Fe-oxides, including Fe_4O_5, Myhill et al. (2016) provided an estimate of the thermodynamic properties of the $Mg_2Fe_2O_5$ endmember primarily based on Mg–Fe^{2+} partitioning between $(Mg,Fe)_2Fe_2O_5$ and olivine solid solutions reported by Woodland et al. (2013). Experiment Z1461o, conducted at 1300 °C and 16 GPa, produced a three-phase assemblage of $MgFe_2O_5$ coexisting with Fe_2O_3 and MgO, indicating that it lies essentially on phase boundary defined by the equilibrium $Mg_2Fe_2O_5 = 2\,MgO + Fe_2O_3$ (Table 1). This P–T point, along with further constraints on the position of this phase boundary as depicted in Fig. 3 of Uenver-Thiele et al. (2017a) allow us to refine the standard enthalpy ($H°_{298}$) of $Mg_2Fe_2O_5$ in combination with new data for the equation of state of this material from Siersch et al. (2017) and molar volume reported here. The thermodynamic properties of MgO and Fe_2O_3 were taken from the dataset of Holland and Powell (2011), as suggested by Myhill et al. (2016). The properties of $Mg_2Fe_2O_5$ are given in Table 6, along with their sources. The heat capacity was derived from the molar sum of the heat capacities of MgO and $MgFe_2O_4$, as compiled by Holland and Powell (2011). The study of Uenver-Thiele et al. (2017a) demonstrated that their data for these two phases (along with that of hematite) reproduce the experimentally determined position of the breakdown reaction $MgFe_2O_4 = MgO + Fe_2O_3$ reasonably well over a temperature range of ~400 °C. From our analysis, we obtain $H°_{298} = -1981.5$ kJ mol^{-1} for $Mg_2Fe_2O_5$. This result is ~5 kJ mol^{-1} less negative than that previously estimated by Myhill et al. (2016). The small amount of Mg present in the coexisting hematite [0.0618(9) Mg cations on a three-oxygen basis], as reported by Uenver-Thiele et al. (2017a) in experiment Z1461o translates to a $X_{Fe2O3} = 0.979$. Assuming ideal mixing, this slight deviation from pure hematite contributes an uncertainty of only ~300 J at the conditions of the experiment.

Mg–Fe partitioning between $(Mg,Fe)_2Fe_2O_5$ and silicate phases

The partitioning of Mg and Fe^{2+} indicates that $(Mg,Fe)_2Fe_2O_5$ has a strong preference for Fe^{2+} compared to coexisting silicate phases (Fig. 9). This behaviour was also observed by Woodland et al. (2013), but we can now extend this to majoritic garnet and phase B. Defining $K_D = X^{\text{silicate}}_{Fe^{2+}} \times X^{O_5}_{Mg} \Big/ X^{\text{silicate}}_{Mg} \times X^{O_5}_{Fe^{2+}}$, we obtain $K_D^{\text{grt}/O_5} = \sim 0.09$ and $K_D^{\text{phB}/O_5} = \sim 0.05$, respectively, where Fe^{2+} was calculated from stoichiometry (Table 7).

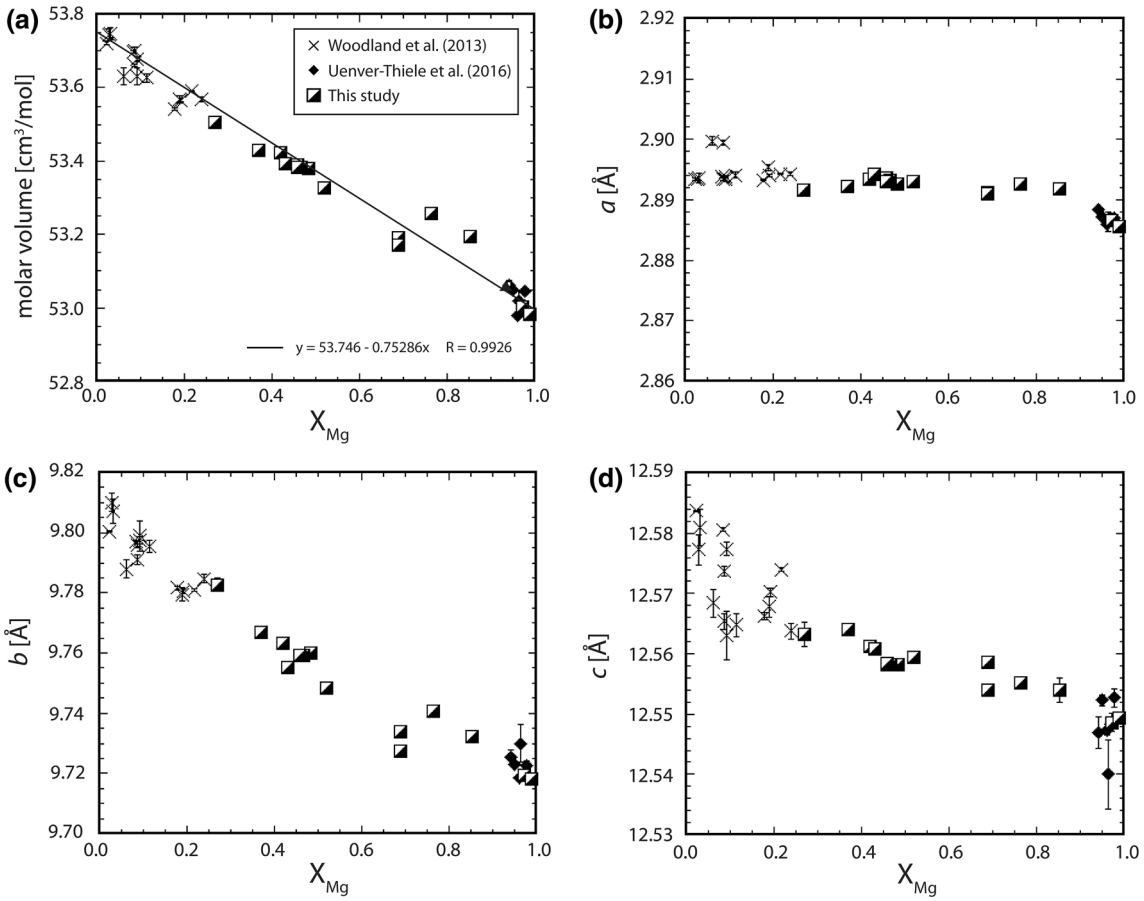

Fig. 8 Variations in **a** molar volume and lattice parameters (**b**–**d**), as a function of X_{Mg} in the O_5-phase. Error bars represent uncertainties obtained from refinement of the powder diffraction patterns using GSAS (Toby et al. 2001). Most errors are the same size or smaller than the symbol

Table 6 Thermodynamic data for $Mg_2Fe_2O_5$

	$Mg_2Fe_2O_5$	Source
$H°_{1bar,298}$ (kJ mol^{-1})	−1981.5	This study
$S°_{298}$ (J K^{-1} mol^{-1})	169.0	Myhill et al. (2016)
$V°_{298}$ (cm^3 mol^{-1})	52.99	This study
K_o (GPa)	171	Siersch et al. (2017)
K′	4	Siersch et al. (2017)
K″ (GPa^{-1})	−2.353 e-2	Myhill et al. (2016)
α_o (K^{-1})	2.36 e-5	Myhill et al. (2016)
Cp (J K^{-1} mol^{-1}) *a*	311.0	Holland and Powell (2011) from molar sum of terms for MgO and magnesioferrite
b	−7.143 e-3	
c	−1.535 e6	
d	−2.3216 e3	

Heat capacity terms have the form: $a+bT+cT^{-2}+dT^{-0.5}$

For partitioning with the Mg–Fe-silicate polymorphs olivine, wadsleyite and ringwoodite, an analogous treatment can be expressed in terms of the exchange reaction:

$$\underset{O_5}{Fe^{2+}Fe^{3+}O_{2.5}} + \underset{ol/wads/rgw}{MgSi_{0.5}O_2} = \underset{O_5}{MgFe^{3+}O_{2.5}} + \underset{ol/wads/rgw}{FeSi_{0.5}O_2} \quad (1)$$

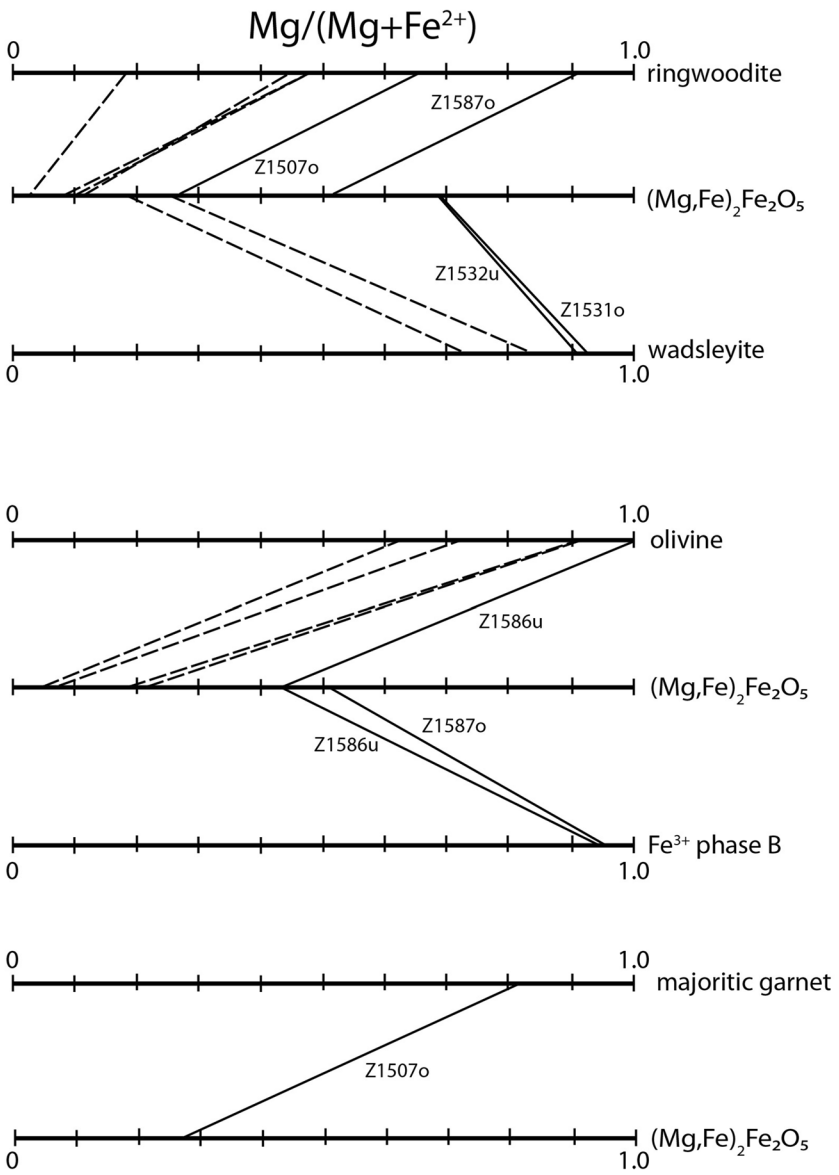

Fig. 9 Mg–Fe^{2+} partitioning between the $(Fe,Mg)_2Fe_2O_5$ and coexisting Si-bearing phases plotted as tie lines in terms of the molar $Mg/(Mg+Fe^{2+})$ of each phase. Data from Woodland et al. (2013) are plotted as dashed tie lines for comparison

The standard state Gibbs free energy of this equilibrium can be expressed as:

$$\Delta G^{\circ}_{(P,T)} = -RT \ln K_D - RT \ln K_{\gamma}, \quad (2)$$

where K_D is defined as above and $K\gamma$ accounts for non-ideal behaviour. Assuming the observed ideal volume of mixing for $(Mg,Fe)_2Fe_2O_5$ solid solutions is representative of general ideal mixing behaviour for this phase, Eq. (2) becomes:

$$\Delta G^{\circ}_{(P,T)} = -RT\ln K_D + W^{\text{silicate}}_{\text{Fe-Mg}} (2X^{\text{silicate}}_{Fe^{2+}} - 1) \quad (3)$$

when taking into account the known non-ideal behaviour of olivine, wadsleyite or ringwoodite, here modelled as symmetric solid solutions. Values for K_D at the P and T of our experiments can be computed by combining standard thermodynamic data for the Fe and Mg-endmembers of silicate phases from Holland and Powell (2011) with data from Myhill et al. (2016, 2017) for Fe_4O_5 and our results for $Mg_2Fe_2O_5$ (Table 6). The interaction parameters, $W^{\text{silicate}}_{\text{Fe-Mg}}$, for olivine (2000 kJ), wadsleyite (7500 kJ) and ringwoodite (4160 kJ) on a single-site basis were taken from Frost (2003). The results of these calculations are presented in Table 7, along with the K_D values obtained from our five new Si-bearing experiments and several samples from Woodland et al. (2013). There is reasonable agreement for partitioning with olivine, supporting our assumption that $(Mg,Fe)_2Fe_2O_5$ solid solutions behave ideally. On the other hand, there are discrepancies in K_D values for Mg–Fe^{2+} partitioning with wadsleyite and ringwoodite, implying that these silicate phases, particularly wadsleyite, should have even higher Mg contents than those measured in the

Table 7 X_{Mg} and X_{Fe2+} as well as calculated partitioning coefficients $[K_D = (X_{Fe}^{silicate} \times X_{Mg}^{O5})/(X_{Mg}^{silicate} \times X_{Fe}^{O5})]$ for silicate phases coexisting with the O_5-phase

Experiment	O_5-phase	ol/wds/rgw		grt/phase B	
	X_{Mg}	X_{Mg}	K_D	X_{Mg}	K_D
		ol		**grt**	
Z1507o	0.265(1)	0.666(3)	0.181(2)	0.807(1)	0.086(1)
Z1531o	0.691(4)	0.927(3)	0.176(8)		
Z1532u	0.688(3)	0.906(3)	0.229(8)		
				Fe-phase B	
Z1587o	0.515(5)	0.908(2)	0.108(3)	0.954(1)	0.051(1)
Z1586u	0.434(8)	0.994(6)	0.005(5)	0.948(2)	0.042(2)
4f3v131[a]	0.091(2)	0.72	0.039		
4f1v127[a]	0.216(14)	0.91	0.027		
8f1v127[a]	0.192(6)	0.9	0.026		
		wds			
4f1h1645[a]	0.187(7)	0.819(12)	0.050(4)		
8f1h1646[a]	0.248(10)	0.829(8)	0.068(4)		
8f1v238[a]	0.238(4)	0.823(4)	0.067(2)		
		rgw			
9f8v232[a]	0.029(2)	0.181(6)	0.135(10)		

O_5-phase $(Mg,Fe)_2Fe_2O_5$, *ol* olivine, *wds* wadsleyite, *rgw* ringwoodite, *grt* garnet

[a]Data from Woodland et al. (2013)

experimental run products (Table 7). For ringwoodite, the differences in K_D are fairly small, on the order of ~0.04–0.05 and a likely explanation is that the presence of Fe^{3+} influences Mg–Fe^{2+} partitioning. This effect is not expected for olivine due to the lack of significant Fe^{3+} incorporation into this phase (e.g., Koch et al. 2004). Similar small differences are also observed for wadsleyite-bearing experiments of Woodland et al. (2013). However, samples Z1531o and Z1532u from this study both exhibit much larger differences in calculated and observed K_D (Table 7). These differences are even much larger than can be accounted for by considering the effect of strongly non-ideal interactions between the Mg_2SiO_4 and $(Fe^{3+}_{5/3}\square_{1/3})Fe^{3+}O_4$ components in wadsleyite ($W^{wadsleyite}_{Fe^{3+}-Mg} = 20$ kJ) as described by Frost and McCammon (2009) for oxidizing conditions (Re–ReO_2 buffer). However, the work of Mrosko et al. (2015) suggests that our results may be due to the combination of Fe^{3+} and OH incorporation in wadsleyite. Thus, we attribute the differences in calculated and observed K_D to the presence of Fe^{3+} and OH in wadsleyite. However, it is clear from the K_D values presented in Table 7 that the O_5-phase will always have the highest Fe content in mantle-relevant assemblages.

Redox stability of $(Mg,Fe)_2Fe_2O_5$ solid solutions

A number of experiments reported in Table 1 contain a $(Mg,Fe)_2Fe_2O_5$ solid solution coexisting with hematite, which allows us to estimate the oxygen fugacity (fO_2) of equilibration via the equilibrium:

$$Fe^{2+}{}_2Fe^{3+}{}_2O_5 + 0.5\ O_2 = 2\ Fe_2O_3, \quad (4)$$

where

$$\Delta G^{\circ}_{(P,T)} = -RT\ln K = -2RT\ln a^{hem}_{Fe_2O_3} + RT\ln a^{O_5}_{Fe_4O_5} + 0.5RT\ln fO_2 \quad (5)$$

From the very limited deviation in hematite composition from the pure Fe_2O_3 as described above, we can reasonably assign unit activity of Fe_2O_3 for this phase. This, along with the assumption of ideal mixing on sites in $(Mg,Fe)_2Fe_2O_5$ (i.e., $a = X^2$) and rearranging yields the following simplification to Eq. 5:

$$\Delta G^{\circ}_{(P,T)} - 2RT\ln(X^{O_5}_{Fe^{2+}}) = 0.5RT\ln fO_2 \quad (6)$$

The fO_2 can then be computed by combining compositional data from this study and from Uenver-Thiele et al. (2017b) with standard state thermodynamic data for hematite, Fe_4O_5 and O_2 from Holland and Powell (2011), Myhill et al. (2016) and Stagno and Frost (2010), respectively. The systematics of equilibrium (4) relative to the Re–ReO_2 and the metastable fayalite–magnetite quartz (FMQ) oxygen buffers are illustrated in Fig. 10 as a function of pressure at 1300 and 1500 °C. Also plotted are the results of the few samples that were equilibrated at these two temperatures. As expected, the experiments employing PtO_2 to minimize the formation of Fe^{2+} record the highest fO_2, lying about 5 log units above FMQ. Somewhat lower fO_2 values are computed for the two experiments where no PtO_2 was added and partial reduction of Fe^{3+} occurred (M519, M566; Fig. 10; Table 2). Unsurprisingly the lowest fO_2 values are calculated for the experiments with the $Mg_{0.5}Fe_{0.5}Fe_2O_4$ starting composition, where $Fe^{3+}/\sum Fe = 0.8$. However, our experiments with coexisting $(Mg,Fe)_2Fe_2O_5$ and hematite were clearly performed under strongly oxidizing conditions, as was intended for investigating the behaviour of Fe^{3+} under deep mantle conditions. Although such conditions are much more oxidizing than generally expected for the deep upper mantle and transition zone (e.g., Frost and McCammon 2009), this does not exclude their appearance due to local excursions to high oxygen fugacities through interactions with subducted material or migrating carbonatite melts. These regions, where redox gradients occur, may also be important for the crystallization of diamond (Stachel et al. 1998).

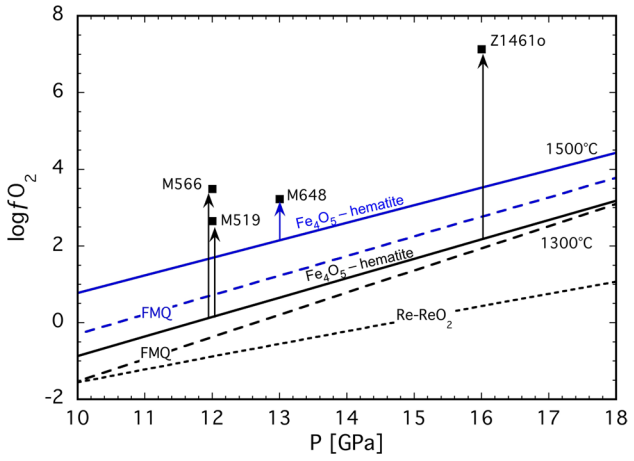

Fig. 10 logfO_2 of the equilibrium between $Fe^{2+}{}_2Fe^{3+}{}_2O_5$ and hematite plotted against pressure at 1300 and 1500 °C along with values calculated for several samples run at the same temperatures. The arrows indicate the shift in logfO_2 related to Mg incorporation in Fe_4O_5. Also shown for reference are the positions of the metastable FMQ and Re–ReO_2 redox buffer equilibria (Ballhaus et al. 1991; Myhill et al. 2016, 2017)

Concluding remarks

Combining the results on the crystal-chemical behaviour of Fe_4O_5–$Mg_2Fe_2O_5$ solid solutions of this study with those of Uenver-Thiele et al. (2017a, b) and Woodland et al. (2013), it is apparent that complete solid solution exists across the binary join. A steady decrease in molar volume with increasing Mg content indicates ideal mixing behaviour. The variation in molar volume arises primarily from shortening along the *b*-axis with increasing Mg content. Although our results are in good agreement with the observations of Woodland et al. (2013), our wider compositional range also reveals more subtle changes in the *a*- and *c*-parameters with composition.

The stability of the O_5-phase depends on the phase assemblage and bulk composition. For example, the study of Si-free bulk compositions (Uenver-Thiele et al. 2017a, b) demonstrates that the minimum pressure for $(Mg,Fe)_2Fe_2O_5$ coexisting with hematite is ~ 10–11 GPa at ~ 1500–1600 °C. However, the maximum stability of the O_5-phase in these Si-free systems depends on the redox conditions, and thus, on the Fe^{2+}/Mg ratio of $(Mg,Fe)_2Fe_2O_5$ (compare results of Uenver-Thiele et al. 2017a with b). The endmember assemblage $Mg_2Fe_2O_5 + Fe_2O_3$ remains stable up to 20 GPa, whereas the maximum stability of $Mg_{0.5}Fe_{0.5}Fe_2O_5 + Fe_2O_3$ lies at ~ 14–16 GPa at ~ 1000–1300 °C and decreases to higher temperatures. This contrasts with the results of the Si-bearing experiments where hematite is absent. Here, $(Mg,Fe)_2Fe_2O_5$ can be stabilized down to depths corresponding to the lower transition zone (~ 20 GPa) under more reducing conditions, consistent with the results of Myhill et al. (2016) who found Fe_4O_5 to be stable to at least 22 GPa.

In Si-bearing bulk compositions, $(Mg,Fe)_2Fe_2O_5$ can occur, even though it does not incorporate Si into its structure, consistent with previous studies (e.g., Woodland et al. 2013; Bindi et al. 2016). The new experiments reported here demonstrate that the list of known Si-phases with which $(Mg,Fe)_2Fe_2O_5$ can coexist (olivine, wadsleyite, ringwoodite, spinelloid V or clinopyroxene; Woodland et al. 2013) can now be extended to include majoritic garnet and Fe^{3+}-bearing phase B. Chemical analyses of the garnet (Z1507o) indicate a composition of 82 mol% $(Mg,Fe)_4Si_4O_{12}$ and 18 mol% $(Mg,Fe)_3Fe_2Si_3O_{12}$. Since phase B with the chemical formula $Mg_{12}Si_4O_{19}(OH)_2$ is known to become stable under hydrous conditions, its presence in our "dry" experiments was surprising, particularly since no PtO_2 was added to these experiments that could have been a source of adsorbed H_2O. Raman spectra obtained from phase B confirmed the presence of some structural water as OH; however, further quantification of the exact amount of OH by infrared spectroscopy or secondary ion mass spectrometry (SIMS) is required. A possible explanation for the stabilization of phase B might be the incorporation of Fe^{3+}, which is reported here for the first time. EPMA and EDX measurements in the TEM gave consistent results with a composition of $Mg_{11.17(4)}Fe_{1.04(6)}Si_{3.79(3)}O_{21}H_2$. Additional Fe-L ELNES analysis yielded a $Fe^{3+}/\sum Fe = \sim 0.41(4)$, confirming that Fe^{3+} entered the structure via the charge-balanced substitution: $^{[4]}Si^{4+} + {}^{[6]}Mg^{2+} = 2Fe^{3+}$. Based on the fact that phase B can not only store water, but also can accommodate Fe^{3+} and Fe^{2+} makes this hydrous magnesium silicate even more interesting as a possible mantle phase. From only two experiments, we have little constraint on the *P*–*T* stability of Fe^{3+}-bearing phase B, except that it appears to be stable between at least 14 and 20 GPa at fairly low temperature (Table 3). An analogous substitution involving Cr^{3+} was recently reported for anhydrous phase B (Bindi et al. 2016; Sirotkina et al. 2017). Assuming the crystal chemistry of phase B and anhydrous phase B is similar with respect to substitution of trivalent cations, the incorporation of Cr^{3+} and Fe^{3+} together has the potential for expanding the stability field of phase B, particularly in terms of redox conditions. The same situation also holds for $(Mg,Fe)_2Fe_2O_5$ in that the substitution of other trivalent cations (i.e., Cr and Al) will act to stabilize this phase to lower oxygen fugacities and also to a potentially wider range of pressures and temperatures, making it even more relevant for the mineralogy of the deep upper mantle and transition zone. The incorporation of such cations will also expand the range of bulk compositions in which the O_5-phase can be stable. Investigation of such solid solutions is currently underway.

Acknowledgements This work was supported by the Deutsche Forschungsgemeinschaft through grants WO 652/20-1 and BO 2550/7-1 to ABW and TBB, respectively. E. Alig is thanked for helping with obtaining the X-ray powder diffraction patterns. We are grateful to Thomas Kautz, Nicki Siersch and Svyatoslav Shcheka for their help with the multi-anvil experiments at the University of Frankfurt and the Bayerisches Geoinstitut. Heidi Höfer is thanked for her help with the microprobe analysis. We also acknowledge the comments by Bob Myhill and two anonymous reviewers which helped to improve the manuscript.

References

Armstrong JT (1993) Matrix correction program CITZAF, Version 3.5. California Institute of Technology

Ballhaus C, Berry RF, Green DH (1991) High pressure experimental calibration of the olivine–orthopyroxene–spinel oxygen geobarometer: implications for the oxidation state of the upper mantle. Contrib Mineral Petrol 107:27–40

Bindi L, Sirotkina EA, Bobrov A, Nestola F (2016) Chromium solubility in anhydrous phase B. Phys Chem Miner 43:103–110

Boffa Ballaran T, Uenver-Thiele L, Woodland AB, Frost DJ (2015) Complete substitution of Fe^{2+} by Mg in Fe_4O_5: the crystal structure of the $Mg_2Fe_2O_5$ end-member. Am Mineral 100:628–632

Brey GP, Bulatov V, Girnis A (2008) Geobarometry for peridotites: experiments in simple and natural systems from 6 to 10 GPa. J Petrol 49:3–24

Enomoto A, Kojitani H, Akaogi M, Miura H, Yusa H (2009) High-pressure transitions in $MgAl_2O_4$ and a new high-pressure phase of $Mg_2Al_2O_5$. J Solid State Chem 182:389–395

Finger LW, Ko J, Hazen RM, Gasparik T, Hemley RJ, Prewitt CT, Weidner DJ (1989) Crystal chemistry of phase B and an anhydrous analogue: implications for water storage in the mantle. Nature 341:140–142

Frost DJ (2003) The structure and sharpness of $(Mg,Fe)_2SiO_4$ phase transformations in the transition zone. Earth Planet Sci Lett 216:313–328

Frost DJ, McCammon CA (2008) The redox state of Earth's mantle. Annu Rev Earth Planet Sci 36:389–420

Frost DJ, McCammon CA (2009) The effect of oxygen fugacity on the olivine to wadsleyite transformation: Implications for remote sensing of mantle redox state at the 410 km seismic discontinuity. Am Mineral 94:872–882

Guignard J, Crichton WA (2014) Synthesis and recovery of bulk Fe_4O_5 from magnetite, Fe_3O_4. A member of a self-similar series of structures for the lower mantle and transition zone. Mineral Mag 78:361–371

Guyot F, Boyer H, Madon M, Velde B, Poirier JP (1986) Comparison of the Raman microprobe spectra of $(Mg,Fe)_2SiO_4$ and Mg_2GeO_4 with olivine and spinel structures. Phys Chem Miner 13:91–95

Holland TJB, Powell R (2011) An improved and extended internally consistent thermodynamic dataset for phases of petrological interest, involving a new equation of state for solids. J Metamorph Geol 29:333–383

Ishii T, Kojitani H, Tsukamoto S, Fujino K, Mori D, Inaguma Y, Tsujino N, Yoshino T, Yamazaki D, Higo Y, Funakoshi K, Akaogi M (2014) High-pressure phase transitions in $FeCr_2O_4$ and structure analysis of new post-spinel $FeCr_2O_4$ and $Fe_2Cr_2O_5$ phases with meteoritical and petrological implications. Am Mineral 99:1788–1797

Ishii T, Kojitani H, Fujino K, Yusa H, Mori D, Inaguma Y, Matsushita Y, Yamaura K, Akaogi M (2015) High-pressure high-temperature transitions in $MgCr_2O_4$ and crystal structures of new $Mg_2Cr_2O_5$ and post-spinel $MgCr_2O_4$ phases with implications for ultrahigh-pressure chromitites in ophiolites. Am Mineral 100:59–65

Jacob DE, Piazolo S, Schreiber A, Trimby P (2016) Redox-freezing and nucleation of diamond via magnetite formation in the Earth's mantle. Nat Commun 7:11891

Katsura T, Ito E (1989) The system Mg_2SiO_4-Fe_2SiO_4 at high pressures and temperatures: precise determination of stabilities of olivine, modified spinel, and spinel. J Geophys Res 94:15663–15670

Keppler H, Frost DJ (2005) Introduction to minerals under extreme conditions. In: Miletich R (ed) Mineral behaviour at extreme conditions, vol 7. EMU Notes in Mineralogy, pp 1–30

Koch M, Woodland AB, Angel RJ (2004) Stability of spinelloid phases in the system Mg_2SiO_4–Fe_2SiO_4–Fe_3O_4 at 1100 °C and up to 10.5 GPa. Phys Earth Planet Inter 143:171–183

Larson AC, Van Dreele RB (1994) GSAS general structure analysis system. Los Alamo National Laboratory, New Mexico

Lavina B, Meng Y (2015) Unraveling the complexity of iron oxides at high pressure and temperature: synthesis of Fe_5O_6. Sci Adv 1(5):e1400260

Lavina B, Dera P, Kim E, Meng Y, Downs RT, Weck PF, Sutton SR, Zhao Y (2011) Discovery of the recoverable high-pressure iron oxide Fe_4O_5. Proc Natl Acad Sci 108:17281–17285

Liu L-G, Lin C-C, Mernagh TP, Irfune T (1998) Raman spectra of phase B at various pressures and temperatures. J Phys Chem Solids 59:871–877

McMillan P, Akaogi M (1987) Raman spectra of β-Mg_2SiO_4 (modified spinel) and ɣ-Mg_2SiO_4 (spinel). Am Mineral 72:361–364

McMillan PF, Akaogi M, Sato RK, Poe B, Foley F (1991) Hydroxyl groups in β-Mg_2SiO_4. Am Mineral 76:354–360

Mrosko M, Koch-Müller M, McCammon CA, Rhede D, Smyth JR, Wirth R (2015) Water, iron, redox environment: effects on the wadsleyite–ringwoodite phase transition. Contrib Mineral Petrol 170:9

Myhill B, Ojwang DO, Ziberna L, Frost D, Boffa Ballaran T, Miyajima N (2016) On the P–T–fO_2 stability of Fe_4O_5 and Fe_5O_6-rich phases: a thermodynamic and experimental study. Contrib Mineral Petrol 171:1–11

Myhill B, Ojwang DO, Ziberna L, Frost D, Boffa Ballaran T, Miyajima N (2017) Correction to: on the P–T–fO_2 stability of Fe_4O_5 and Fe_5O_6-rich phases: a thermodynamic and experimental study. Contrib Mineral Petrol 171:51

Siersch NC, Boffa Ballaran T, Uenver-Thiele L, Woodland AB (2017) Compressibility and high-pressure structural behavior of $Mg_2Fe_2O_5$. Am Mineral 102:845–850

Sinmyo R, Bykova E, Ovsyannikov SV, McCammon C, Kupenko I, Ismailova L, Dubrovinsky L (2016) Discovery of Fe_7O_9: a new iron oxide with a complex monoclinic structure. Sci Rep 6:32852

Sirotkina EA, Bobrov AV, Bindi L, Irifune T (2017) Chromium-bearing phases in the Earth's mantle: evidence from experiments in the Mg_2SiO_4–$MgCr_2O_4$ system at 10–24 GPa and 1600 °C. Am Mineral 103:151–160

Stachel T, Harris JW, Brey GP (1998) Rare and unusual mineral inclusions in diamond from Mwadui, Tanzania. Contrib Mineral Petrol 132:34–47

Stagno V, Frost DJ (2010) Carbon speciation in the asthenosphere: experimental measurements of the redox conditions at which carbonate-bearing melts coexist with graphite or diamond in peridotite assemblages. Earth Planet Sci Lett 300:72–84

Temple PA, Hathaway CE (1973) Multiphonon spectrum of silicon. Phys Rev B 7:3685

Toby BH (2001) EXPGUI, a graphical user interface for GSAS. J Appl Crystallogr 34:210–213

Uenver-Thiele L, Woodland AB, Boffa Ballaran T, Miyajima N, Frost DJ (2017a) Phase relations of $MgFe_2O_4$ at conditions of the deep upper mantle and transition zone. Am Mineral 102:632–642

Uenver-Thiele L, Woodland AB, Boffa Ballaran T, Miyajima N, Frost DJ (2017b) Phase relations of Fe–Mg spinels including new high-pressure post spinel phases and implications for natural samples. Am Mineral 102:2054–2064

Van Aken PA, Liebscher B (2002) Quantification of ferrous/ferric ratios in minerals: new evaluation schemes of Fe L_{23} electron energy-loss near-edge spectra. Phys Chem Miner 29:188–200

Van Aken PA, Liebscher B, Styrsa VJ (1998) Quantitative determination of iron oxidation states in minerals using Fe $L_{2,3}$-edge electron energy-loss near edge structure spectroscopy. Phys Chem Miner 25:323–327

Woodland AB, Frost DJ, Trots DM, Klimm K, Mezouar M (2012) In situ observation of the breakdown of magnetite (Fe_3O_4) to Fe_4O_5 and hematite at high pressures and temperatures. Am Mineral 97:1808–1811

Woodland AB, Schollenbruch K, Koch M, Boffa Ballaran T, Angel RJ, Frost DJ (2013) Fe_4O_5 and its solid solutions in several simple systems. Contrib Mineral Petrol 166:1677–1686

Woodland AB, Uenver-Thiele L, Boffa Ballaran T (2015) Synthesis of Fe_5O_6 and the high-pressure stability of Fe^{2+}–Fe^{3+}-oxides related to Fe_4O_5. Goldschm Abstr 2015:3446